

# Multi-approach Electron Paramagnetic Resonance Investigations of UV-Photoinduced $\text{Ti}^{3+}$ in Titanium Oxide-Based Gels

Bruno Pattier,<sup>†</sup> Mark Henderson,<sup>†</sup> Andreas Pöpl,<sup>‡</sup> Abdelhadi Kassiba,<sup>\*,†</sup> and Alain Gibaud<sup>†</sup>

Laboratoire de Physique de l'Etat Condensé, UMR CNRS 6087, Université du Maine, 72085 Le Mans Cedex 09, France, Fakultät für Physik und Geowissenschaften, Universität Leipzig, Linnéstrasse 5, D-04103 Leipzig, Germany

Received: November 30, 2009; Revised Manuscript Received: February 22, 2010

EPR investigations of the photoreduction of  $\text{Ti}^{4+}$  into  $\text{Ti}^{3+}$  under UV irradiation were carried out on three titanium-based materials for which the initial concentration of  $\text{Ti}^{4+}$  was defined in the ternary phase diagram ( $\text{TiOCl}_2$ ,  $\text{H}_2\text{O}$ , DMF). The kinetics of this photoreduction was monitored at 200 K and related to the initial concentration of  $\text{Ti}^{4+}$  in the solution. This study was complemented by a multi-approach EPR method (pulsed electron paramagnetic resonance (EPR), pulsed electron nuclear double resonance, and hyperfine sublevel correlation spectroscopy (HYSCORE)) with the aim of probing the proton environment of the  $\text{Ti}^{3+}$  ions. Indeed, many species such as  $\text{H}_2\text{O}$ ,  $\text{OH}^-$ ,  $\text{HCOO}^-$  are located in the immediate vicinity of  $\text{Ti}^{3+}$ . Although we found that a distribution of  $g$  tensors was involved, for simplicity, two types of  $g$  tensor were used to describe the main features of the EPR signal related to the paramagnetic ions. Additionally, we have evidenced that two kinds of protons are identified next to  $\text{Ti}^{3+}$  species, with specific distances determined from the hyperfine coupling parameters obtained by the HYSCORE method.

## I. Introduction

Among inexpensive promising materials that can be used for photovoltaic applications,  $\text{TiO}_2$  is definitely one of the most attractive.<sup>1</sup> Not only can it be used in its anatase form to make dye-sensitive solar cells,<sup>2</sup> but also it has obvious capabilities for the photoremediation of pollutants and for water catalysis.<sup>3</sup> In its gel form, titanium is remarkable in the sense that it can form photoinduced electrons localized as  $\text{Ti}^{3+}$  centers.<sup>4–8</sup> The mechanism of the  $\text{Ti}^{3+}$  formation is well-described by a series of chain reactions starting with the creation of photoinduced electron–hole pairs. The latter produces, on the one hand, radicals by the reaction of holes with surrounding oxygen entities and, on the other hand, the transformation of  $\text{Ti}^{4+}$  into  $\text{Ti}^{3+}$  paramagnetic centers under the localization of a conduction band at the surface of the colloidal titanium based particles. In this state, the gel exhibits a strong absorption continuum covering the UV–visible–IR spectral range.

To monitor and understand the formation of  $\text{Ti}^{3+}$  species, electron paramagnetic resonance (EPR) is a key technique. Indeed,  $\text{Ti}^{4+}$  is in a nonparamagnetic state, whereas  $\text{Ti}^{3+}$  is an active EPR center. It is therefore possible to monitor in situ the formation of  $\text{Ti}^{3+}$  ions under UV irradiation by measuring the EPR signal of  $\text{Ti}^{3+}$ . Previous experiments have already shown how EPR studies can bring information on the surfacic  $\text{Ti}^{3+}$  species in the presence of suitable hole scavengers.<sup>8–11</sup> It is clearly pinpointed that the properties of the gel depend on the mode of preparation of the colloidal particles.<sup>12–14</sup>

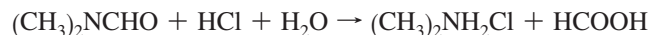
In this paper, the kinetics of the photoinduced transformation of  $\text{Ti}^{4+}$  into  $\text{Ti}^{3+}$  is investigated and analyzed. Samples were selected in the ternary phase diagram ( $\text{TiOCl}_2$ ,  $\text{H}_2\text{O}$ , DMF) with increasing initial concentration of  $\text{Ti}^{4+}$ . They were irradiated under UV light to promote the photoreduction of  $\text{Ti}^{4+}$  to  $\text{Ti}^{3+}$ .

Multi-approach EPR experiments were then performed to analyze the features of the involved paramagnetic centers (nature of paramagnetic radicals, environments). Beyond continuous wave (CW) EPR experiments, field-sweep electron spin echo (FS ESE), hyperfine sublevel correlation spectroscopy (HYSCORE), and pulsed electron nuclear double resonance (ENDOR) techniques<sup>15</sup> were used to probe the local environments of the  $\text{Ti}^{3+}$  ions. The FS ESE measurements show the coexistence in all samples of two different  $\text{Ti}^{3+}$  species characterized by different  $g$  tensors and relaxation times ( $T_M$ ). The influence of the water content on the coordination environments of the photoinduced  $\text{Ti}^{3+}$  centers was also monitored by using the HYSCORE and pulsed ENDOR experiments. On the basis of these approaches, two types of proton signals were detected in the near environments of  $\text{Ti}^{3+}$  with quite different hyperfine coupling tensors. Thus, quantitative estimations of the proton distances with respect to the central  $\text{Ti}^{3+}$  ions were performed, and assignments of the protons in the first coordination shell of  $\text{Ti}^{3+}$  ions are then discussed.

## II. Experimental Details

**a. Material Engineering.** Gels were made from  $\text{TiOCl}_2$ , which is stable in acidic conditions, and from dimethylformamide (DMF) according to a process patented by L. Brohan et al.<sup>16</sup> DMF acts as a solvent but also promotes gel formation by consuming hydrochloric acid.

The hydrolysis of DMF in acidic conditions yields the formation of dimethylammonium chloride and formic acid according to the following scheme:

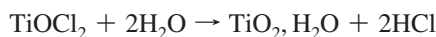


The consumption of HCl drives the instability of  $\text{TiOCl}_2$  that hydrolyzes and condenses into a titanium oxide gel according to the following reaction:

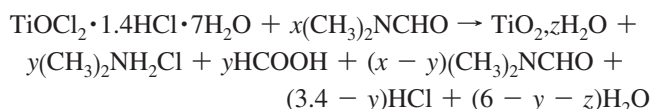
\* Corresponding author. E-mail: kassiba@univ-lemans.fr.

<sup>†</sup> Université du Maine.

<sup>‡</sup> Universität Leipzig.



The entire process can be summarized as:



This reaction is quite slow and can be thermally activated by heating the solution at 70 °C for 24 h. According to this chemical process, the final composition of the gel can be tuned by varying the amount of water and DMF in the initial reactants. Gels were made under argon flow and at various concentrations of  $\text{TiOCl}_2$ , water, and DMF. Their composition inferred from the initial masses of reactants is represented in the ternary phase diagram shown in Figure 1. For simplicity, the diagram is drawn by considering  $\text{TiOCl}_2$  and HCl as a unique entity.

The study was carried out at a fixed weight percentage of  $\text{TiOCl}_2$  and HCl and variable amounts of DMF and water. The final gel with concentrations of  $\text{Ti}^{4+}$  of 0.98, 1.10, and 1.26 M are referred to below as A, B and C, respectively. The synthesis uses a given volume of HCl (2 M) mixed with 5.36 g of a titanium oxychloride and 10 mL of DMF. To vary the initial concentration of  $\text{Ti}^{4+}$ , the volume of HCl was 4, 2, and 0 mL for samples A, B, and C, respectively.

These different solutions were prepared under anaerobic conditions and in an ice bath to prevent the evaporation of HCl. They were then transferred into quartz EPR tubes under argon prior to gelification achieved by heating at 70 °C for 24 h.

The morphology and microstructure of the different titanium-based gels were investigated by small-angle X-ray scattering (SAXS) using the Swing beamline at the third generation French synchrotron radiation facility SOLEIL.

**b. Instrumental Set-up.** CW EPR measurements were carried out with a Bruker EDX spectrometer operating at 9.4 GHz and 2 mW at 200 K. The  $g$  factor was calibrated by reference to a sample of 1,1-diphenyl-2-picrylhydrazyl (DPPH,  $g = 2.0037 \pm 0.0002$ ). The normalization of the number of spins related to the EPR signal intensity was performed by reference to the EPR signal of a freshly prepared copper sulfate solution. The samples were irradiated in situ using a UV lamp (365 nm, 3.5 mW  $\text{cm}^{-2}$ ) for approximately 24 h. The irradiation was performed also on other samples of the same composition at room temperature using a 200 W Hg lamp for 24 h.

Investigations by multi-approach techniques using pulsed EPR were carried out on an X-band Bruker ELEXYS E580 spectrometer. Beyond traditional cw-EPR, which identifies and quantifies the features of the paramagnetic centers (PC), pulsed EPR methods such as HYSORE and pulsed ENDOR<sup>15</sup> probe the interaction of PCs with the nuclei in the first and higher coordination shells. The FS ESE spectra were measured with a two-pulse echo sequence with microwave (mw) pulse lengths of  $t_{\pi/2} = 16$  ns and  $t_{\pi} = 32$  ns with different pulse delays of  $\tau = 120$  and 800 ns at 8 K. HYSORE experiments<sup>17</sup> were performed using the pulse sequence  $(\pi/2_{\text{mw}} - \tau - \pi/2_{\text{mw}} - t_1 - \pi_{\text{mw}} - t_2 - \pi/2_{\text{mw}} - \tau - \text{echo})$  with nonselective mw pulse of  $t_{\pi/2} = 16$  and  $t_{\pi} = 32$  ns at 16 K. Pulse delays of  $\tau = 32, 64, 104, 136,$  and 168 ns were chosen to minimize blind spots in the HYSORE powder pattern. In the cases of  $\tau = 32$  and 64 ns, the HYSORE echo was detected via a remote echo sequence  $(\pi/2_{\text{mw}} - t_{\text{R}} - \pi/2_{\text{mw}} - t_{\text{R}} - \pi_{\text{mw}} - t_{\text{R}} - \text{echo})$ , since the dead time of the spectrometer exceeds 64 ns in our experimental setup. The pulse delays of the remote echo sequence were  $t_{\text{R}} =$

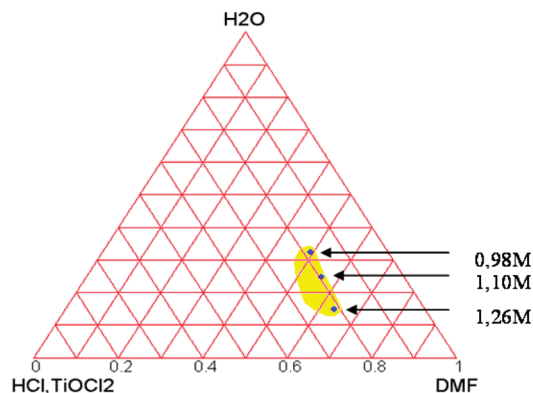


**Figure 1.** Schematic representation of the mass ternary phase diagram with the three compositions considered in this study. Outside the yellow area, the gel is turbid.

4  $\mu\text{s}$  and  $\tau_{\text{R}} = 140$  ns. A four-step phase cycle suggested by Gemperle et al.<sup>18</sup> was used to avoid interference with the unwanted two- and three-pulse echoes. A 2D data matrix (170  $\times$  170) was sampled with a dwell time of 16 ns. The baseline correction was performed by subtracting a third-order polynomial of the experimental data set in both time domains. No apodization functions were employed in processing of the 2D spectra to avoid additional broadening. Finally, the HYSORE spectra recorded with different  $\tau$  values were added, and the 2D FT magnitude spectra were calculated and presented as contour plots.

Pulsed ENDOR spectra were measured using the Davies ENDOR sequence<sup>19</sup> characterized by  $(\pi_{\text{mw}} - \pi_{\text{rf}} - \pi/2_{\text{mw}} - \tau - \pi_{\text{mw}} - \tau - \text{echo})$  with selective mw pulses of  $t_{\pi/2, \text{mw}} = 96$  ns and  $t_{\pi, \text{mw}} = 192$  ns and a radio frequency (rf) pulse length of  $t_{\pi, \text{rf}} = 8 \mu\text{s}$  at 8 K.

### III. Kinetics of the Photoinduced Reduction of $\text{Ti}^{4+}$ into $\text{Ti}^{3+}$

**a. EPR Spectrum Features under UV-Irradiation.** During the sample irradiation, the color of the different samples changes from transparent to blue or dark blue. This is the consequence of the photoinduced conversion of  $\text{Ti}^{4+}$  (spinless ion) into  $\text{Ti}^{3+}$  (paramagnetic ion,  $S = 1/2$ ). This conversion can be followed by EPR spectroscopy. With this in mind, appropriate instrumental parameters (modulation field, microwave power, detection frequency, etc.) were selected to avoid any saturation phenomena or distortion of any kind on the EPR line shapes. Figure 2a shows typical EPR spectra for increasing UV irradiation times. As expected, no signal is measured when the gel is not irradiated due to the absence of paramagnetic species. Under UV irradiation, the EPR signal quickly increases over a short period before leveling off at a longer time. The growth of the intensity in the EPR spectra is a direct consequence of the appearance of paramagnetic centers. EPR signals are generally fitted using a dedicated powder program with  $S = 1/2$ , anisotropic  $g$  tensor, and suitable line widths and shapes. However, due to the weak  $g$  tensor anisotropy, the EPR spectra can be described by a superposition of two derivatives of Lorentzian lines that are quite close in position (Figure 2b). The following analytical expression was used to define the intensity of a given derivative Lorentzian line,

$$I(H) = -\frac{32 \times I_0 \times \Delta H \times (H - H_{\text{r}})}{(3 \times \Delta H^2 + 4 \times (H - H_{\text{r}})^2)^2}$$

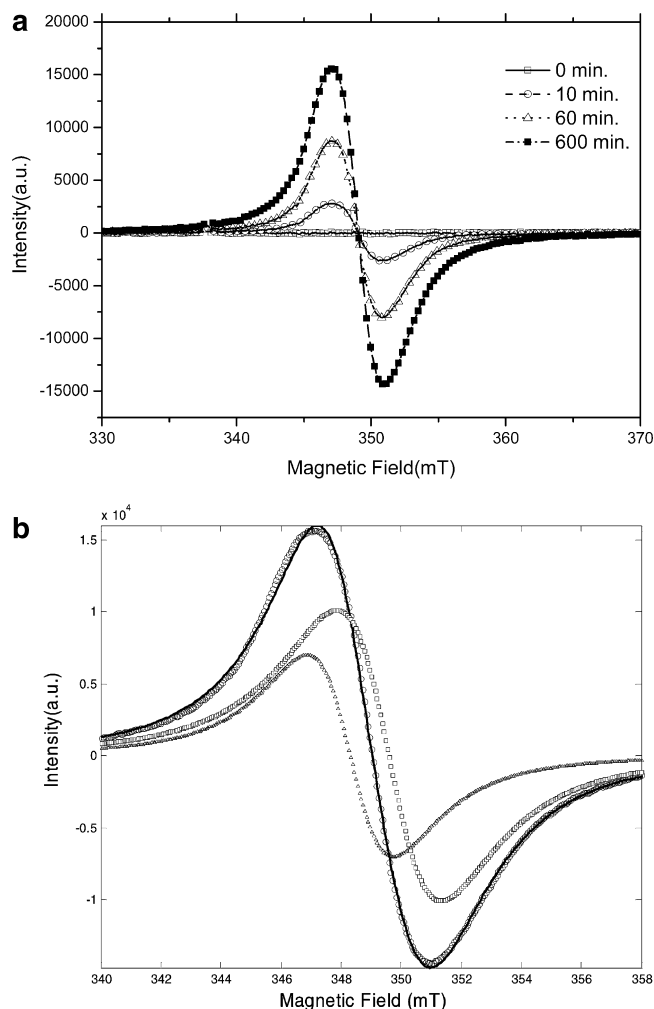


**Figure 2.** (a) Evolution of EPR signal in function of UV irradiation time at 200 K. (b) Decomposition of the EPR spectrum into two derivatives of Lorentzian lines.

where  $H_r$  is the center position,  $\Delta H$  is the full width peak to peak, and  $I_0$  is the maximum intensity.

The fitting was carried out via a homemade program written in Matlab. At each irradiation time, the  $g$  factors, the width and the amplitude related to the two main components of the EPR signal, were determined (Figures 3 and 4). The analysis of the main features is hereafter addressed following the sample composition as defined above in the phase diagram.

**b. Interpretation of the Results.** The line widths and  $g$  factors of gel A are depicted in Figure 3a, b. For gel A, the line widths increase slightly with the irradiation time due to an increase in the spin concentration through the conversion of  $Ti^{4+}$  to  $Ti^{3+}$ . Dipole–dipole interaction can contribute to the line broadening, depending on the distance between interacting spins. For the same reason, the shifts of the line position can be induced by local fields around spin probes when the concentration of spins increases. The axial  $g$  tensor of  $Ti^{3+}$  in the gel medium did not show any noticeable variation of the anisotropy with the irradiation time. Both  $g$  tensor components vary in the same way as a function of time. The intensity of the EPR signal reported in Figure 4 shows that sample A exhibits the largest  $Ti^{3+}$  concentration as compared to the two other investigated samples. This indicates that the  $Ti^{4+} \rightarrow Ti^{3+}$  conversion is more efficient in the diluted system.

For gels B and C, only slight variations of the spectral parameters with the irradiation time were noticed. This behavior

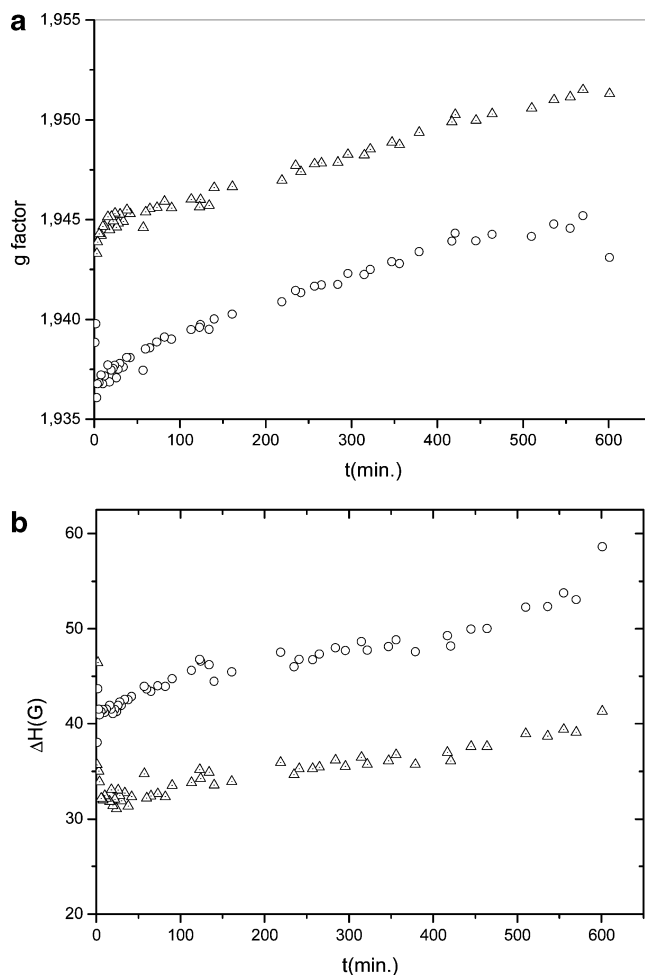


**Figure 3.** Time evolution of line-position ( $g$  factor) and line width for the EPR signal in A gel (a, b). The large time evolution is shown in the spectral parameters of the EPR spectra in the sample with more water content (A).

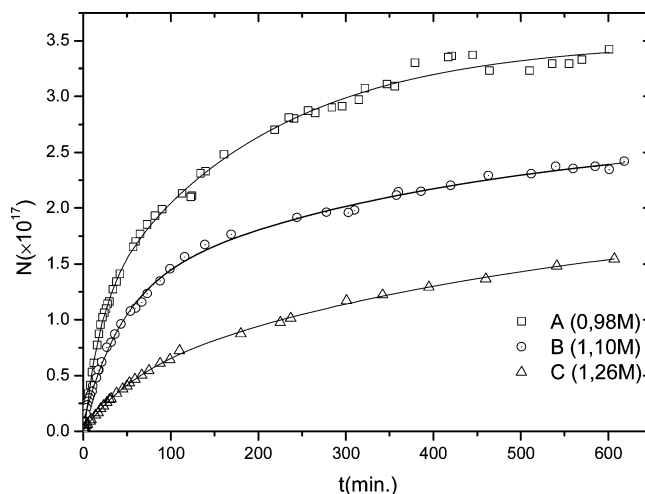


**Figure 4.** Intensity evolutions vs 366 nm irradiation time.

is consistent with a lower number of paramagnetic centers created by the UV irradiation, as shown on the EPR signal intensity after long exposure time (Figure 4). These results contrast with the fact that the initial content of titanium is larger in samples B and C as compared to sample A. Such behavior can be explained by assuming that the kinetics of the photoinduced conversion and the efficiency of the process are dependent on the microstructure of the gel or the water content, as

**TABLE 1: Absolute Concentration of UV-Photinduced  $\text{Ti}^{3+}$  under 366 nm Irradiation Line or under the Full Hg Spectrum in the Investigated Samples (A, B, C) Which Differ by the  $\text{Ti}^{4+}$  Molarity (M)**

	initial composition $\text{Ti}^{4+}$ (M)	366 nm irradiation			full Hg spectrum irradiation		
		$\tau_1$ (min)	$\tau_2$ (min)	$Y_{\max}$	$\tau_1$ (min)	$\tau_2$ (min)	$Y_{\max}$
A	0.98	18	192	$3.5 \times 10^{17}$	16	101	$4.9 \times 10^{17}$
B	1.10	43	399	$2.7 \times 10^{17}$	21	99	$9.2 \times 10^{17}$
C	1.26	54	524	$2.0 \times 10^{17}$	26	570	$2.9 \times 10^{18}$

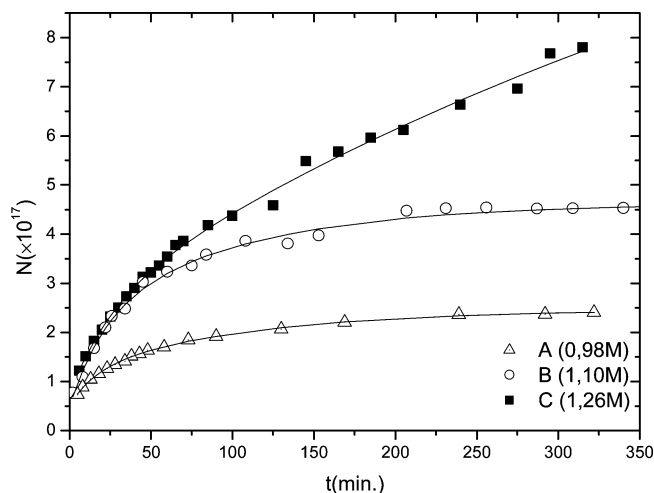
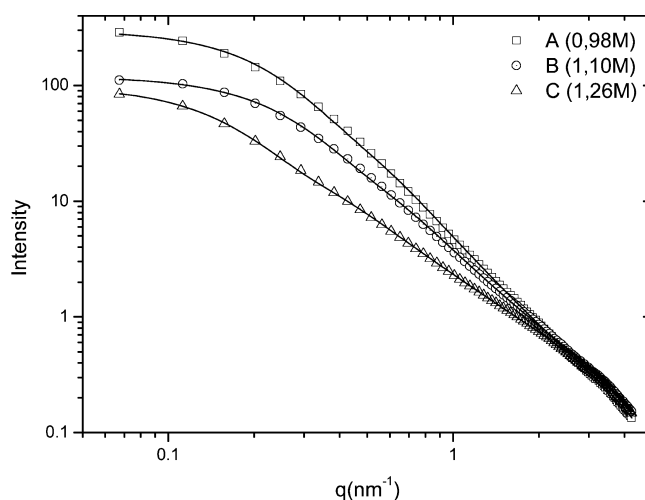
discussed below. However, for all samples, the  $g$  factors are quite close, with  $g_1 = 1.945$  and  $g_2 = 1.935$ . The EPR line widths that bring the mark of relaxation and interaction phenomena are in the range of 40 and 30 gauss and slightly increase with the time of irradiation. No hyperfine coupling (hfc) was shown on the EPR spectra. Regarding the line width  $\sim 40$  Gauss and the hyperfine interaction parameters  $\sim 36$  Gauss,<sup>5</sup> the absence of any details from the hyperfine structure indicates delocalized electrons from the titanium ions. The residence probability of unpaired electrons in the 3d orbital is then low enough to overcome any resolved signal from the hyperfine structure.

The EPR intensity curves for the three samples depicted in Figure 4 reflect the time evolution of the  $\text{Ti}^{3+}$  concentration during the irradiation time. At first glance, the number of  $\text{Ti}^{3+}$  spins can be fitted by using double exponential terms according to the following analytical expression,

$$N = N_{\max} - N_1 e^{-t/\tau_1} - N_2 e^{-t/\tau_2}$$

where  $\tau_1$  and  $\tau_2$  are characteristic time constants,  $t_0$  is a time delay, and  $N$  represents the number of spins, which is deduced from double integration of the EPR signal associated with each titanium-based gel and compared with a reference sample (Figure 4 and Table 1).

The time constants (Table 1), which characterize the kinetics of photogeneration of  $\text{Ti}^{3+}$ , were attributed to the process of photogeneration of electrons and holes ( $h^+$ ,  $e^-$ ) followed by their transformations mainly by a trapping process ( $\text{Ti}^{4+} + 1e^- \rightarrow \text{Ti}^{3+}$ ).<sup>11</sup> Because two quite different time constants were necessary to account for the kinetics, it is thought that two mechanisms should be involved. The short time constant characterizes direct trapping of photogenerated electrons by the  $\text{Ti}^{4+}$ , whereas the longer time constant is related to some diffusion of free charge carriers in the gel network and some possible recombination with scavenger species such as oxygen. Because the kinetic is highly dependent on the irradiation energy density, the creation of the  $\text{Ti}^{3+}$  ions occurs first at the surface of the gel directly exposed to the UV beam. Deeper centers involved inside the gel are created, but with longer time constant with respect to the decrease in the beam intensity inside the material. It is worth noting that alternatively to the two characteristic times used to traduce the time dependent kinetics of  $\text{Ti}^{3+}$  creation, the use of the model of Kohlrausch–Williams–Watts with nonexponential relaxation works also. This model accounts for a mechanism in which a distribution of time constants occurs due to local fluctuations of the gel composition or its density. The interaction matter–radiation in the gel bulk then proceeds as different local environments are involved around the titanium ions, as can be suggested by the exhaustive EPR line features analysis carried out on the selected samples.

**Figure 5.** Intensity evolutions vs full spectrum Hg lamp irradiation time.**Figure 6.** Scattering intensity experimental curve data and fitted for gels A, B, and C.

On the other hand, the kinetics is clearly faster for samples with a low concentration of  $\text{Ti}^{4+}$ . This is quite counterintuitive, since a simple approach would yield a rate of transformation proportional to the initial concentration of  $\text{Ti}^{4+}$ , which is the opposite of what is observed. However, the measurements performed with the full Hg mercury lamp spectrum reveal that the kinetics stay faster at lower concentrations (Figure 5) but the higher intensity of the EPR signal obtained for a long exposure time correlates with the concentration, as can be expected. Furthermore, the difference of the maximum of EPR in the A and C gels is no longer proportional to the initial  $\text{Ti}^{4+}$  concentration. To understand the features of the kinetics of photoinduced charge conversion and time evolution, microstructure investigations were carried out by the SAXS technique. The results point out that the particles which compose the three investigated gels exhibit greater size with the increase in the initial  $\text{Ti}^{4+}$  concentration.

As shown in Figure 6, the SAXS intensity at small wave vectors,  $q$ , saturates at a lower value for gel C, followed by that in gel B, and the highest intensity is realized for the low-concentration gel (A). All the intensity curves merge at the same point at high  $q$ , showing that the slope in the fractal regime (typically from 0.2 to 1.5  $\text{nm}^{-1}$ ) decreases when the concentration increases. The fractal dimension for the three gels is found to be 2.5, 2.2, and 1.7, respectively, for gels A, B, and C. This



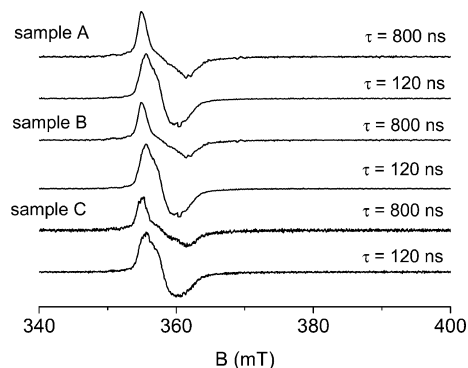


**Figure 7.** First derivatives of the FS ESE spectra of samples A, B, and C measured at 8 K and with different pulse delays,  $\tau$ .

means that the density of the gels decreases from gel A to C gel, and the size of the homogeneous domains decreases from the gel C to gel A, as seen by the location of the curvature in the scattering intensities. We can therefore conclude that gel A is denser with smaller particles as compared to gel C, which is made from larger objects but with less density of matter. In addition, if we assume that the photo conversion of  $\text{Ti}^{4+}$  into  $\text{Ti}^{3+}$  occurs at the surface of objects, we may understand why gel A leads to a faster kinetic and to a higher conversion rate as compared to C gel. The main reason is related to the specific surface, which is more important for gel A, gel B and finally for C gel. After the long exposure time and when the process is complete, the microstructures in all gels exhibit similar features, leading then to the proportionality between the final EPR line intensity of  $\text{Ti}^{3+}$  and the initial concentration of  $\text{Ti}^{4+}$ .

In the forthcoming sections, multi-approach EPR experiments are performed with the aim of identifying the local near environments of the  $\text{Ti}^{3+}$  ions.

#### IV. Pulsed EPR Studies of Titanium Oxide-Based Gels

The studied samples differ by the water content 4 (sample A), 2 (sample B), and 0 mL (sample C). All samples were initially irradiated for 24 h. The effect of such a treatment is seen on the color of the samples, changing from transparent to dark blue. Before measurements that were carried out after several days of irradiation, all samples were illuminated by the full spectrum of a high-pressure mercury arc lamp at room temperature for about 3 min. Upon illumination, the more or less transparent samples turned dark blue immediately. Then, FS ESE, HYSCORE, and pulsed ENDOR experiments were performed to explore the local environment of the UV-photoinduced  $\text{Ti}^{3+}$  and the role of water dilution on the  $\text{Ti}^{3+}$  environment.

**a. Two-Pulse FS ESE Measurements.** Samples A, B, and C show intense  $\text{Ti}^{3+}$  ESE signals at about  $g = 1.94$ . Figure 7 illustrates the first derivatives of the corresponding FS ESE spectra, which were recorded with two different pulse delays,  $\tau = 120$  and 800 ns. In all samples, the presence of at least two components is observed at 356 and 360 mT. The relative intensity of the signal component at 356 mT seems to increase with rising pulse delays,  $\tau$ , in comparison with the second major signal component at 360 mT. Therefore, both signals have different phase memory relaxation times,  $T_M$ , and cannot be interpreted in terms of just a single anisotropic  $\text{Ti}^{3+}$  species. We must rather assume that two different  $\text{Ti}^{3+}$  species with  $g$  values of  $g_1 = 1.945$  ( $\text{Ti}^{3+}(1)$ ) and  $g_2 = 1.935$  ( $\text{Ti}^{3+}(2)$ ) having different  $T_M$  relaxation times exist in the illuminated gel samples, in accordance with the deconvolution of their corresponding

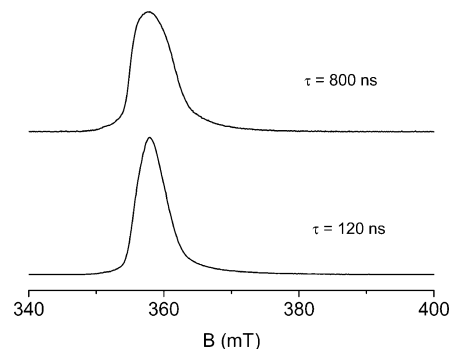


**Figure 8.** FS ESE spectra of sample A measured at 8 K and with different pulse delays,  $\tau$ .

cw EPR spectra (Figures 2 and 3). However, a close inspection of the original FS ESE spectra before the calculation of the first derivatives reveals a very broad anisotropic  $\text{Ti}^{3+}$  FS ESE spectrum that extends up to  $\sim 380$  mT, corresponding to  $g$  values of about  $g_{zz} \approx 1.82$ . As an example, the original FS ESE spectra of sample A are shown in Figure 8. Therefore, the  $\text{Ti}^{3+}$  centers have presumably highly anisotropic  $g$  tensors with a broad distribution of  $g_{zz}$  principal values. Then, the observed signal components with  $g_1 = 1.945$  and  $g_2 = 1.935$  correspond to the  $g_{xx,yy}$  spectral components of the two  $\text{Ti}^{3+}$  centers.

In general, the line shapes differ in the FS ESE spectra recorded with  $\tau = 120$  and 800 ns. The  $\tau = 800$  ns spectra reveal a larger anisotropy of the  $\text{Ti}^{3+}$  powder patterns. This indicates that species with longer  $T_M$  relaxation times provide spectra with larger anisotropy. Thus, we may conclude that we do not form two unique  $\text{Ti}^{3+}$  species by the illumination, but rather, a broad variety of  $\text{Ti}^{3+}$  species having different  $g$  tensors and, consequently, different coordination environments. The distribution of the  $g$  tensor components seems to be centered at the  $g_{xx,yy}$  spectral components  $g_1 = 1.945$  and  $g_2 = 1.935$ . Therefore, it seems justified to restrict our further studies to these two components assigned to the species  $\text{Ti}^{3+}(1)$  and  $\text{Ti}^{3+}(2)$ .

**b. HYSCORE and Pulsed ENDOR Measurements.** Detailed HYSCORE and pulsed ENDOR experiments were carried out on sample A; that is, the sample with the highest  $\text{H}_2\text{O}$  content. The HYSCORE spectra were measured with different pulse delays,  $\tau = 32, 64, 104, 136$ , and 168 ns, to minimize blind spots in the modulation patterns. The presented spectra were then obtained by adding the individual spectra recorded for the various  $\tau$  values.

Intense  $^1\text{H}$  cross-peak signals are observed in the HYSCORE spectrum of sample A recorded at 362.6 mT and corresponding to the spectral position of the  $\text{Ti}^{3+}$  center  $\text{Ti}^{3+}(2)$  (Figure 9). Modulations from other nuclei have not been observed. In the experimental 2D spectrum (Figure 9a and c) we distinguish two types of proton signals, I and II. Signal I is assigned to a cross-peak ridge pattern close to the proton nuclear Larmor frequency extending from (13.6, 17.4) MHz to (17.4, 13.6) MHz (Figure 9a). The cross peak ridges of signal I are overlapped by an intense signal at the  $^1\text{H}$  nuclear Larmor frequency at 15.4 MHz due to distant matrix protons. On the basis of spectral simulations,<sup>20</sup> we estimate the hfc parameters of proton I to the values  $A(I)_{xx,yy} = -4.1$  MHz,  $A(I)_{zz} = 2.8$  MHz, which translate into isotropic and anisotropic hfc parameters  $A(I)_{\text{iso}} = -1.8$  MHz and  $T(I)_{\perp} = 2.3$  MHz, respectively. The angle  $\beta$  between the  $g_{zz}$  and  $A(I)_{zz}$  axes is close to  $90^\circ$ .

In the simulation, we assumed that the selected field position corresponds to the  $g_{xx,yy}$  spectral position of EPR spectrum of

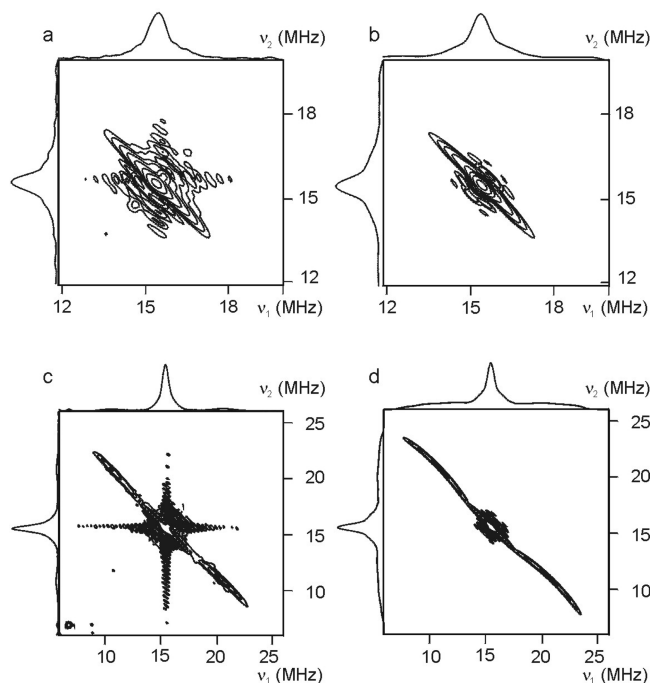
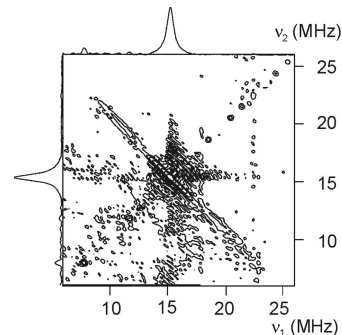


**Figure 9.** Experimental (a, c) and simulated (left) HYSCORE spectra of sample A recorded at 16 K at 362.6 mT. The displayed spectra are the sum of five different spectra sampled with different pulse delays,  $\tau = 32, 64, 104, 136,$  and  $168$  ns.

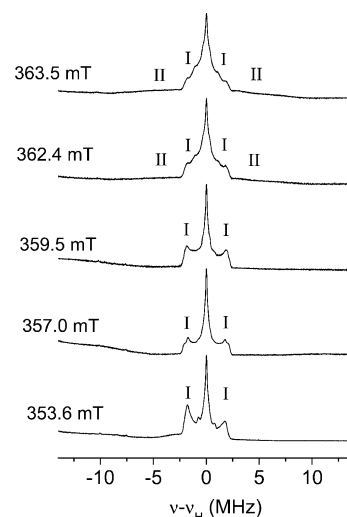
the titanium species  $\text{Ti}^{3+}(2)$ . The simulated spectrum is displayed in Figure 9b. The peak at the  $^1\text{H}$  nuclear Larmor frequency of the distant matrix protons was simulated by using the HYSCORE spectra of 10 weakly coupled protons with hfc parameters  $A_{\text{iso}} = 0$  and  $T_{\perp} = 0.3$  MHz and adding this spectrum to those of proton I. The angle  $\beta$  close to  $90^\circ$  indicates that proton I is located close to the  $g_{xx,xx}$  plane of the  $\text{Ti}^{3+}$  ions, suggesting that it can be assigned to an equatorially coordinating ligand. The dipolar coupling parameter  $T_{\perp}$  as estimated from the simulations translates into a titanium–proton distance of about 0.33 nm using a simple point dipole approximation.<sup>15</sup> Such a proton–titanium distance is typical for a proton in the third coordination shell of an equatorial ligand. Thus, proton I could be assigned to an HCOO ligand, as recently suggested by Cottineau et al.<sup>8</sup>

Figure 9c shows the same HYSCORE spectrum, but on an extended scale. The spectrum displays two more cross-peak ridges of the second proton, II. Its ridges are less intense in comparison with those of proton I, but they are much more extended and range from (22.1, 9.3) MHz to (9.3, 22.1) MHz, indicating a substantially larger proton hf interaction. The hfc parameters  $A(\text{II})_{xx,yy} = 3.8$  MHz,  $A(\text{II})_{zz} = 16.8$  MHz,  $A(\text{II})_{\text{iso}} = 8.1$  MHz,  $T(\text{II})_{\perp} = 4.3$  MHz, and  $\beta \approx 90^\circ$  for proton II have been estimated from spectral simulations in which we likewise assumed that the selected observer field position corresponds to the  $g_{xx,yy}$  spectral position of the  $\text{Ti}^{3+}(2)$  center. As for proton I, the angle  $\beta$  indicates that proton II is also located close to the  $g_{xx,yy}$  plane of the  $\text{Ti}^{3+}$  ion and can be assigned to an equatorially coordinating ligand. The dipolar coupling parameter  $T_{\perp}$  translates into a titanium–proton distance of 0.26 nm using a simple point dipole approximation. This distance would be in accordance with an equatorially coordinating  $\text{H}_2\text{O}$  or OH ligand.<sup>21</sup> Therefore, we assume that the titanium center  $\text{Ti}^{3+}(2)$  possesses a mixed  $\text{H}_2\text{O}/\text{OH}$  and HCOO ligand environment.

Although the signal-to-noise ratio is considerably worse for the HYSCORE spectrum of sample A recorded at 358.4 mT



**Figure 10.** Experimental HYSCORE spectrum of sample A recorded at 16 K at 358.4 mT. The displayed spectrum is the sum of five different spectra sampled with different pulse delays  $\tau = 32, 64, 104, 136,$  and  $168$  ns.



**Figure 11.** Experimental Davies ENDOR spectra of sample A recorded at 8 K. The roman numerals I and II indicate ENDOR signal components from protons I and II, respectively.

and corresponding to the spectral position of the second titanium center  $\text{Ti}^{3+}(1)$  (Figure 10), the cross-peak ridges of protons I and II could be likewise observed. However, the relative intensity of the extended cross-peak ridge of proton II in comparison to those of proton I in the spectrum of species  $\text{Ti}^{3+}(1)$  seems to be less as compared to the spectrum taken from the center  $\text{Ti}^{3+}(2)$ . Therefore, the number of coordinating  $\text{H}_2\text{O}/\text{OH}$  moieties in comparison to HCOO ligands seems to be lower for  $\text{Ti}^{3+}(1)$ .

Davies ENDOR spectra measured on sample A at different field positions (Figure 11) support the results of the HYSCORE experiments. The selected observer fields cover the spectral range of the  $g_{xx,yy}$  spectral positions of both titanium species,  $\text{Ti}^{3+}(1)$  and  $\text{Ti}^{3+}(2)$ . In general, pulsed ENDOR spectroscopy provides a better spectral resolution for nuclei with smaller hfc, such as proton I in comparison to the HYSCORE experiments, and is complementary to this method to some extent. The presented ENDOR spectra in Figure 11 show, in addition to the matrix ENDOR line from distant protons at the  $^1\text{H}$  Larmor frequency, a  $^1\text{H}$  ENDOR doublet with a splitting of about 4 MHz. This doublet can be assigned to the  $A(\text{I})_{xx,yy}$  component of the powder ENDOR pattern of proton I, which belongs to the HCOO ligands. These signals from protons I are present in the ENDOR spectra for all observer field positions. At 357.0 mT, a splitting of the ENDOR doublet seems to indicate a small orthorhombic distortion of the hfc tensor of proton I. In addition, the ENDOR spectra reveal a further very broad proton ENDOR

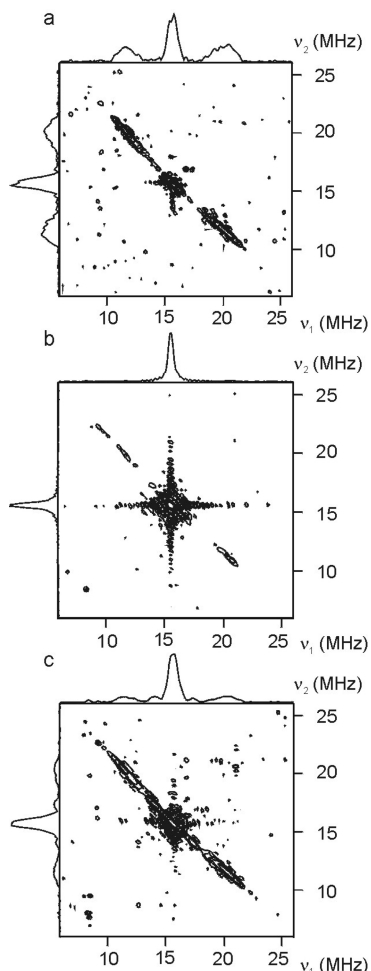


**Figure 12.** Experimental HYSCORE spectra of samples (a) A, (b) B, and (c) C recorded at 16 K at 362.6 mT with a pulse delay of  $\tau = 136$  ns.

signal covering a range of  $\sim 17$  MHz. This corresponds to the  $A(\text{II})_{zz} = 16.8$  MHz principal value of proton II, and we may assign this broad powder ENDOR signal to the equatorial coordinating OH or  $\text{H}_2\text{O}$  ligands. The broad ENDOR response of proton II is in particular obvious in the spectra recorded at 363.5 and 362.4 mT. At these two observer field positions, the  $g_{xx,yy}$  spectral parameters of the titanium species  $\text{Ti}^{3+}(2)$  dominates the EPR powder pattern. Therefore, the average number of OH or  $\text{H}_2\text{O}$  ligands in comparison to the HCOO ligands should be higher for species  $\text{Ti}^{3+}(2)$  in comparison to  $\text{Ti}^{3+}(1)$ . It is worth noting that this conclusion is in accordance with the HYSCORE results presented above.

Additional HYSCORE experiments were performed on samples B and C to probe the influence of the water content on the coordination environment of the photoinduced  $\text{Ti}^{3+}$  centers. The spectra were recorded at 326.6 mT, where the major contribution to the HYSCORE signals is caused by the species  $\text{Ti}^{3+}(2)$ . The experiments were performed with only one pulse delay,  $\tau = 136$  ns, which is optimal to enhance the most characteristic spectral features of both protons I and II in the HYSCORE spectrum. Figure 12 compares the spectra from samples B and C with a spectrum of sample A likewise recorded with  $\tau = 136$  ns at 326.6 mT. All three spectra display the characteristic cross-peak ridges of protons I and II from the equatorially coordinating HCOO and OH/ $\text{H}_2\text{O}$  species, respectively. However, the relative ratio between the proton signals I and II seem to vary among the three samples. The signal from

proton II of the strongly coupled  $\text{H}_2\text{O}$  or OH ligands is most intense for sample A with 4 mL of  $\text{H}_2\text{O}$ , but is very weak in the case of sample B with 2 mL of  $\text{H}_2\text{O}$ . However, it does not seem to be a clear trend with the amount of water in the sample.

## V. Summary and Conclusion

Extensive studies were performed to analyze, on one hand, the kinetics of the UV-photoinduced titanium reduction process in titanium-based gels with three selective compositions in the ternary phase diagram ( $\text{TiOCl}_2$ ,  $\text{H}_2\text{O}$ , and DMF). On the other hand, multi-approach EPR investigations were conjugated to characterize the EPR signal features with the aim of judiciously probing the local environments of the photoinduced  $\text{Ti}^{3+}$ .

Thus, the carried out analyses of the kinetics of the photoinduced  $\text{Ti}^{3+}$  ions under UV irradiation and at low power show that the characteristic times and the efficiency of the charge conversion are not correlated to the initial  $\text{Ti}^{4+}$  content in the samples and even present some counterintuitive behavior. The efficiency of the photoconversion is higher in sample A (low concentration), followed by samples B and, finally, C. As a support of such an analysis, we may note that the instrumental EPR parameters are marked by the slight increase in both the line widths and  $g$  tensor components with the irradiation time exclusively for sample A. This is mainly a consequence of the large concentration of the photoinduced  $\text{Ti}^{3+}$  in sample A, in agreement with the large specific surface, leading to the efficiency of surface titanium reduction. In addition, when a large concentration of paramagnetic species is involved with an appropriate distance between paramagnetic centers, it is usual to have exchange interactions between spins, which can lead to an increase in the line width and also to shifts of the EPR line positions.<sup>22–25</sup>

The observed behavior of the conversion efficiency in the considered samples was searched through their microstructures. Particularly, high specific areas favor the presence of more surface-like titanium, which can be a source of the photogenerated  $\text{Ti}^{3+}$ . To quantify this possibility, a good correlation exists between the efficiency of the  $\text{Ti}^{3+}$  photogeneration and the specific surface measured by X-ray diffraction. This was fully justified from the experiments carried out by SAXS method.

The multi-approach experiments based on continuous and pulsed EPR and ENDOR spectroscopy allow probing the symmetry and local environment around the photoinduced  $\text{Ti}^{3+}$  in the titanium-based gels. The photogeneration of ( $e^-$ ,  $h^+$ ) under UV-irradiation and the electron trapping at the  $\text{Ti}^{4+}$  sites leads to  $\text{Ti}^{3+}$  centers ( $3d^1$ ,  $S = 1/2$ ) which are active in EPR. In all investigated samples, two  $\text{Ti}^{3+}$  species, 1 and 2, with  $g_{xx,yy} = 1.945$  ( $\text{Ti}^{3+}(1)$ ) and  $g_{xx,yy} = 1.935$  ( $\text{Ti}^{3+}(2)$ ) have been observed upon illumination. The  $g_{zz}$  ( $\sim 1.82$ ) principal values of both species are smaller than  $g_{xx,yy}$  but appear to be widely distributed, as revealed by the FS ESE experiments. Whatever the sample, the features of the  $g$  tensors are no longer modified by the sample molarity, and similar local environments seem involved, irrespective of the water content. The relation  $g_{xx,yy} > g_{zz}$  implies  $\text{Ti}^{3+}$  ions with  $3d_{xy}$  as the ground state, which would correspond to a tetragonally compressed octahedral crystal field. HYSCORE and pulsed ENDOR measurements revealed further details about the coordination environment of the  $\text{Ti}^{3+}$  species. Hyperfine couplings from protons in the second and third coordination sphere of equatorially coordinating ligands could be detected and suggest a mixed ligand environment around the two titanium centers,  $\text{Ti}^{3+}(1)$  and  $\text{Ti}^{3+}(2)$ . The involved proton I at a distance of 0.33 nm from the titanium ion is assigned to the equatorially

coordinating  $\text{HCOO}^-$  ligand. For proton II with a Ti–H distance of 0.26 nm, its assignment is related to  $\text{H}_2\text{O}$  or OH species binding equatorially to the titanium centers; however, the ligand environment is not uniform for both  $\text{Ti}^{3+}$  species with regard to the average relative number of  $\text{H}_2\text{O}$  or OH ligands higher for the  $\text{Ti}^{3+}(2)$  center as compared to  $\text{Ti}^{3+}(1)$ .

Finally, the EPR spectra of  $\text{Ti}^{3+}$  are relatively narrow with respect to the gel media, where a distribution of local environment or composition fluctuations can cause line broadening. It seems that the gels in such studies appear as well-organized media, leading to paramagnetic centers characterized by quite sharp resonance lines. However, in some experiments, broad features are shown at low temperature (sample A at 6 K) and can be attributed to nonorganized media with a large distribution of local environments around  $\text{Ti}^{3+}$  or, alternatively, to different phase memory relaxation times, as was clearly demonstrated by pulsed EPR experiments.

**Acknowledgment.** The authors are greatly indebted to F. Meneau for assistance at the Swing beamline of SOLEIL and for providing access to the synchrotron. They are greatly indebted to the ANR for providing funds under the project PV OxTi MiB and the Région of Pays de la Loire for a grant attribution in the framework of the PERLE project.

## References and Notes

- (1) Kalayanasundaram, K.; Gratzel, M. *Coord. Chem. Rev.* **1998**, *77*, 347.
- (2) Hagfeldt, A.; Gratzel, M. *Acc. Chem. Res.* **2000**, *33*, 269.
- (3) Fujishima, A.; Honda, K. *Nature* **1972**, *238*, 37.
- (4) Bityurin, N.; Znaidi, L.; Marteau, P.; Kanaev, A. *Chem. Phys. Lett.* **2003**, *367*, 690.
- (5) Castellano, F. N.; Stipkala, J. M.; Friedman, L. A.; Meyer, G. J. *Chem. Mater.* **1994**, *6*, 2123.
- (6) Kameneva, O. V.; Kuznetsov, A. I.; Smirnova, L. A.; Rosez, L.; Sanchez, C.; Kanaev, A.; Alexandrov, A. P.; Bityurin, N. M. *Dokl. Phys.* **2006**, *51*, 103.
- (7) Fadeeva, E.; Koch, J.; Chichkov, B.; Kuznetsov, A.; Kameneva, O.; Bityurin, N.; Sanchez, C.; Kanaev, A. *Appl. Phys. A: Mater. Sci. Process.* **2006**, *84*, 27.
- (8) Cottineau, T.; Brohan, L.; Pregelj, M.; Cevc, P.; Richard-Plouet, M.; Arcon, D. *Adv. Funct. Mater.* **2008**, *18*, 2602.
- (9) Kim, M.; Bray, P. J. *J. Chem. Phys.* **1970**, *53*, 716.
- (10) Howe, R. F.; Grätzel, M. *J. Phys. Chem.* **1987**, *91*, 3906.
- (11) Ke, S. C.; Wang, T. C.; Wong, M. S.; Gopal, N. O. *J. Phys. Chem. B* **2006**, *110*, 11628.
- (12) Coronado, J. M.; Maira, A. J.; Conesa, J. C.; Yeung, K. L.; Augugliaro, V.; Soria, J. *Langmuir* **2001**, *17*, 5368.
- (13) Serpone, N.; Lawless, D.; Khairutdinov, R. *J. Phys. Chem.* **1995**, *99*, 16646.
- (14) Cottineau, T.; Richard-Plouet, M.; Rouet, A.; Puzenat, E.; Sutrisno, H.; Piffard, Y.; Petit, P.-E.; Brohan, L. *Chem. Mater.* **2008**, *20*, 1421.
- (15) Schweiger, A.; Jeschke, G. *Principles of Pulse Electron Paramagnetic Resonance*; Oxford University Press: Oxford, 2001.
- (16) Brohan, L.; Sutrisno, H.; Piffard, Y.; Caldes, M.; Joubert, O. Patent Polymère sol-gel à base de  $\text{TiO}_2$  CNRS-France priorité N° 0201055; 29/01/2002; and Brohan, L.; Sutrisno, H.; Piffard, Y.; Caldes, M.; Joubert, O.; Puzenat, E.; Rouet, A. Polymère sol-gel à base d'oxyde de titane; International publication N° WO 03/064324 A3; 07/08/2003; and European publication (EP) n° 03 734 737.4, 2003.
- (17) Höfer, P.; Grupp, A.; Nebenführ, G.; Mehring, M. *Chem. Phys. Lett.* **1986**, *132*, 279.
- (18) Gemperle, C.; Aebli, G.; Schweiger, A.; Ernst, R. R. *J. Magn. Reson.* **1990**, *88*, 241.
- (19) Davies, E. R. *Phys. Lett. A* **1974**, *47A*, 1.
- (20) Pöppl, A.; Hartmann, M.; Böhlmann, W.; Böttcher, R. *J. Phys. Chem. A* **1998**, *102*, 3599.
- (21) Pöppl, A. L.; Kevan, L. *J. Phys. Chem.* **1996**, *100*, 3387.
- (22) Kassiba, A.; Bednarski, W.; Pud, A.; Erien, N.; Makowska-Janusik, M.; Laskowski, L.; Tabellout, M.; Kodjikian, S.; Fatyeyeva, K.; Ogurtsov, N.; Noskov, Y. J. *J. Phys. Chem. C* **2007**, *111*, 11544.
- (23) Pud, A. A.; Tabellout, M.; Kassiba, A.; Korzhenko, A. A.; Rogalsky, S. P.; Shapoval, G. S.; Houzé, F.; Schneegans, O.; Emery, J. R. *J. Mater. Sci.* **2001**, *36*, 3355.
- (24) Kassiba, A.; Hrabanski, R.; Bonhomme, D.; Hader, A. *J. Phys.: Condens. Matter* **1995**, *7*, 3339.
- (25) Tenailleau, C.; Kassiba, A.; Lacorre, P. *J. Phys. Chem. Solids* **2004**, *11*, 1809.

JP911357V